THE ASTROPHYSICAL JOURNAL, 454:106–118, 1995 November 20

RADIO AND EMISSION-LINE JETS IN THE TYPE 2 SEYFERT GALAXY MARKARIAN 1066 (UGC 2456)[1]

GARY BOWER,[2] ANDREW WILSON,[3,4] AND JON A. MORSE
Space Telescope Science Institute, 3700 San Martin Drive, Baltimore, MD 21218;
bower@stsci.edu, awilson@stsci.edu, morsey@stsci.edu

RICHARD GELDERMAN[5] AND MARK WHITTLE[3]
Department of Astronomy, University of Virgina, P.O. Box 3818, Charlottesville, VA 22903;
gelderman@stars.gfsc.nasa.gov, dmw8f@seyfert.astro.virgina.edu

AND

JOHN MULCHAEY[6]
Space Telescope Science Institute, 3700 San Martin Drive, Baltimore, MD 21218
Received 1995 February 9; accepted 1995 June 1

ABSTRACT

Hubble Space Telescope (*HST*) images, ground-based spectroscopy, and a new VLA map of the type 2 Seyfert galaxy Markarian 1066 (UGC 2456) are used to study the morphology, kinematics, and excitation of the ionized gas and its relation to the radio continuum source. The Hα+[N II] image reveals emission from a region 3″ (490 h^{-1} pc, $h = H_0/100$ km s^{-1} Mpc^{-1}) long centered on the nucleus, while the [O III]-emitting gas is concentrated into a bright "jetlike" structure extending 1.″4 (230 h^{-1} pc) NW of the nucleus. Ground-based spectroscopy indicates that both high- and low-excitation components are present in the narrow-line region. The low-excitation emission lines have ratios similar to those of LINERs, trace out a rotation curve with amplitude $\approx$200 km s^{-1}, and probably originate from gas in the galaxy disk. However, relative to this rotation curve, the [O III]-emitting gas is blueshifted NW of the nucleus and redshifted SE of the nucleus. The VLA 3.6 cm map confirms that the radio source is "linear" and resembles a bipolar jet. Both the [O III] and Hα+[N II] distributions align with the radio axis. The highest excitation gas coincides with the NW radio jet. High-excitation gas may also be associated with the SE radio jet, but its line emission is attenuated by obscuration in the foreground galactic disk. We discuss two possible scenarios which can account for the observed association between the high-excitation gas and the radio jet. A nuclear continuum source could emit ionizing photons anisotropically and preferentially along the jet. Alternatively, shocks may form at the boundary between the jet and ambient cloud material and generate ionizing photons *in situ*.

The radio and emission-line jets in Mrk 1066 are approximately aligned with the galaxy's bar in projection on the sky. However, an analysis of a volume-limited sample of Seyfert galaxies indicates no strong alignment between kiloparsec scale stellar bars and $\sim$100 pc scale radio sources.

Subject headings: galaxies: individual (Markarian 1066) — galaxies: jets — galaxies: nuclei — galaxies: Seyfert — radio continuum: galaxies

1. INTRODUCTION

A persistent problem in the study of active galaxies is the origin of the velocity widths of emission lines from high-excitation gas in the narrow-line region. In many Seyfert galaxies, the acceleration of this gas is dominated by the gravitational potential of the galaxy bulge (Whittle 1992a, b). However, observations of some Seyfert galaxies suggest that other processes can also be important in defining the kinematics and morphology of the high-excitation gas. For example, the high-excitation gas tends to be aligned and cospatial with radio continuum emission, especially for those Seyfert nuclei containing "linear" radio sources (e.g., Haniff, Wilson, & Ward 1988). This result implies that radio jets or lobes enhance the line emission. More detailed evidence that linear radio sources interact with the ionized gas includes the following:

1. Substructure (i.e., subpeaks and shoulders) in the [O III] λ5007 profiles is often found near the radio lobes in double or triple sources (Whittle et al. 1988).
2. Structures resembling bow shocks in both the radio continuum and optical emission-line maps have been discovered in M51, NGC 1068, and NGC 3516 (Cecil 1988; Cecil, Bland, & Tully 1988; Miyali, Wilson, & Pérez-Fournon 1992).
3. The radio luminosity is correlated with both the FWHM and luminosity of [O III] λ5007 (e.g., Wilson & Willis 1980; Whittle 1985).
4. A plot of the FWHM of [O III] λ5007 against parameters sensitive to the gravitational potential, such as rotation curve

[1] Based on observations with the NASA/ESA *Hubble Space Telescope*, obtained at the Space Telescope Science Institute, which is operated by the Association of Universities for Research in Astronomy, Inc., under NASA contract NAS5-26555.
[2] Current address: Department of Physics and Astronomy, Johns Hopkins University, Homewood Campus, Baltimore, MD 21218.
[3] Visiting astronomer, Canada-France-Hawaii Telescope, operated by the National Research Council of Canada, the Centre National de la Recherche Scientifique of France, and the University of Hawaii.
[4] Also Astronomy Department, University of Maryland, College Park, MD 20742.
[5] Current address: NASA/Goddard Space Flight Center, Code 681, Greenbelt, MD 20771.
[6] Current address: Carnegie Observatories, 813 Santa Barabara Street, Pasadena, CA 9101.

amplitude, indicates that processes in addition to gravity contribute to the acceleration of ionized gas in Seyfert nuclei with luminous [log L (1415 MHz) (W Hz^{-1}) $\geq$ 22.5; H_0 = 50 km s^{-1} Mpc^{-1}] linear radio sources (Whittle 1992a, b).

Some models have considered interactions between radio components and ambient gas. Expanding or outwardly moving radio components can sweep up and compress ambient gas which can then be photoionized by the central source (Pedlar, Dyson, & Unger 1985; Taylor, Dyson, & Axon 1992). The northeast radio lobe in NGC 1068 may represent synchrotron emission from ambient magnetic fields and cosmic rays which have been compressed by a radiative bow shock formed by a jet colliding with the ambient ISM (Wilson & Ulvestad 1987). Models such as these predict entrainment of gas, the morphological and kinematic signatures of which should be readily detectable.

For these reasons, we have obtained high-resolution optical and radio images and optical spectroscopy of Mrk 1066 (UGC 2456), a Seyfert 2 galaxy for which existing observations suggest a close relationship between the radio and line-emitting gases. Ground-based optical narrowband imaging (Haniff et al. 1988) has revealed a possible double structure in [O III] extending over the central $\approx$3.″3 and aligned in P.A. = 131° $\pm$ 10°. The Hα+[N II] emission has a similar extent and position angle, but does not show any hint of double structure. Ulvestad & Wilson (1989) mapped the linear nuclear radio source and found it to have a jetlike morphology elongated along P.A. = 134° $\pm$ 4°, close to the [O III] axis. In a plot of rotation curve amplitude versus [O III] λ5007 FWHM, Mrk 1066 lies well off the correlation expected if the [O III] λ5007 FWHM, Mrk 1066 lies well off the correlation expected if the [O III] kinematics are governed exclusively by the galaxy's gravitational potential (Whittle 1992a). These earlier works suggest that the radio jet may be responsible for accelerating the high-excitation gas.

Table 1 lists basic data on Mrk 1066, including the morphological type, an estimate of the inclination, the heliocentric recessional velocity, Galactic extinction, adopted distance and scale, radio luminosity, and spectral index between 6 and 20 cm. Whittle (1992c) notes that the estimate of the inclination is uncertain and may be influenced by the presence of the bar. The adopted distance is obtained from the radial velocity corrected to the reference frame of the cosmic background radiation (de Vaucouleurs et al. 1991). Optical images show that Mrk 1066 is elongated in P.A. $\approx$ 143° at the B = 26.5 mag arcsec^{-2} isophote (Mazzarella & Boroson 1993); however, this seems to apply to the bar. Nilson (1973) lists an uncertain estimate of the major axis position angle of 90°. This galaxy contains a bright "hot spot" (which could be a giant H II region; Mazzarella, Bothun, & Boroson 1991; Mazzarella & Boroson 1993) 15.″9 from the nucleus along the SE side of the bar.

TABLE 1

BASIC DATA FOR MARKARIAN 1066

Property	Value	Reference
Morphological type.....	(R)SB(s)0$^+$	1
Inclination	42°:	2
cz (heliocentric).....	3625 km s^{-1}	3
A_B.....	0.55 mag	1
Distance[a].....	34 h^{-1} Mpc	...
Linear scale[a].....	164 h^{-1} pc arcsec^{-1}	...
L_ν (1.5 GHz).....	1.3 $\times$ 10^{22} h^{-2} W Hz^{-1}	4
α_6^{20} ($S_\nu \propto \nu^{-\alpha}$).....	0.83	4

[a] $h = H_0/100$ km s^{-1} Mpc^{-1}.

REFERENCES.—(1) de Vaucouleurs et al. 1991; (2) Whittle 1992c; (3) this paper; see § 3.2; (4) Ulvestad & Wilson 1989.

2. OBSERVATIONS AND REDUCTIONS

2.1. *HST Imaging*

Images of Mrk 1066 were obtained with *HST* on 1992 November 2 with the Planetary Camera (MacKenty et al. 1992) using the same technique as employed for other Seyfert galaxies in our program (Wilson et al. 1993; Bower et al. 1994; Mulchaey et al. 1994). These references list the effective wavelengths and bandpass widths of the filters (F492M, F547, F664N, and F718M), chosen to isolate the emission lines of [O III] $\lambda\lambda$4959, 5007+Hβ and Hα+[N II] $\lambda\lambda$6548, 6583 and their adjacent continua. Long-slit spectroscopy (§ 2.2) shows that [O III] λ5007/H$\beta \approx 4$ in the central 1″, indicating that [O III] emission accounts for $\approx$84% of the total flux from emission lines in the F492M filter. Thus the contribution of Hβ emission to the F492M image is minor but not negligible. Exposure times were 500–600 s with two exposures obtained in each of the on-band filters (F492M and F664N) and one exposure in each of the off-band filters (F547M and F718M). The initial guide star acquisition was maintained throughout all exposures by tracking in fine lock. One star was detected in the images; its position is identical in the six images to $\pm$14 milliarcseconds, confirming that no significant translational shift occurred during the observations. Data reduction was accomplished by following the procedure given in detail by Bower et al. (1994). The central region ($R \leq 1''$) was detected with S/N $\approx$ 20–30 pixel^{-1} in each filter. The accuracy of flat-field calibration is $\sim$5%, as indicated by the dispersion about the mean background sky level. As in Bower et al. (1994), each image was deconvolved using 50 iterations of the Lucy algorithm (Lucy 1974), yielding resolution $\simeq$0.″1. All features in the deconvolved images are also apparent in the images before deconvolution, although with lower contrast. A comparison of the emission-line fluxes in the narrowband images with the long-slit spectroscopy inside a 0.″86 $\times$ 1.″0 aperture aligned with P.A. = 134° shows agreement to within 30%.

The [O III]+Hβ emission-line image was formed by subtracting the 5460 Å continuum image from the on-band image. The choice of off-band filter for the Hα+[N II] image is less straightforward. Our spectrophotometry (§ 2.2) inside a 0.″86 $\times$ 1.″0 aperture, when combined with the *HST*/PC response function (e.g., Bower et al. 1994), indicates that $\approx$14% of the observed F718M flux in this aperture results from redshifted [S II] $\lambda\lambda$6717, 6731, which is at a wavelength near peak transmission in the bandpass (MacKenty et al. 1992). Removing the continuum contribution from the F664N image might be accomplished better using the F547M image instead. Although [O III] λ5007 contributes less than 1% of the observed F547M flux in the 0.″86 $\times$ 1.″0 aperture, the green continuum distribution is not necessarily identical to that of the red continuum near Hα. The F547M image multiplied by the mean continuum ratio F_λ(7160 Å)/F_λ(5460 Å) of 1.46 found in regions with insignificant Hα+[N II] emission would provide a good estimate of the red continuum in the absence of color variations. Since there is no clear advantage to using either the F718M image or the scaled F547M image for continuum subtraction, we constructed Hα+[N II] images using each. Comparing the two resulting Hα+[N II] images demonstrates that the difference is

minor. The peak intensity and total Hα+[N II] flux agree to 9% in the two images. In this paper, we use the Hα+[N II] image obtained with the scaled F547M image for continuum subtraction.

2.2. *Long-Slit Spectroscopy*

Long-slit spectroscopic observations of Mrk 1066 were obtained on two nights in 1987 November using the Herzberg spectrograph and RCA4 CCD at the f/8 focus of the CFHT. On the first night, we obtained an 1800 s exposure in the green using a 1200 l mm^{-1} grating in first order to cover He II λ4686, Hβ, and [O III] λλ4959, 5007 at a dispersion of 0.62 Å pixel^{-1} (resolution ∼90 km s^{-1} FWHM). On the second night, we obtained two 1800 s exposures in the red using an 830 l mm^{-1} grating in first order to cover [O I] λ6300, Hα, [N II] λλ6548, 6584 and [S II] λλ6717, 6731 at a dispersion of 0.75 Å pixel^{-1} (resolution ∼85 km s^{-1} FWHM). Conditions were photometric on both nights, with seeing ∼0.″9 on the first night and ∼1.″1 on the second night. A 0.″86 wide slit was oriented along the axis of the radio source (P.A. = 134°) and the spectra sampled every 0.″43 (70 h^{-1} pc). Standard reduction procedures were followed within IRAF to generate wavelength and flux-calibrated data. Wavelength errors are ∼0.05 Å while flux errors are typical of slit spectroscopy (∼15%).

As a basic check, we summed the central six spatial increments and compared the resulting profiles with the high quality profiles published by Veilleux (1991b, c) which were taken through a 2.″5 × 2.″5 aperture. The profiles, peak velocities, and line widths agree extremely well, although his higher resolution (∼10 km s^{-1}) separates the two components of the nuclear low-ionization lines more cleanly. These two components are separated by ∼0.″5 with a velocity difference of 125 ± 20 km s^{-1} (Veilleux 1991a). Our averaged near-nuclear line fluxes and ratios agree very well with those given by Goodrich & Osterbrock (1983) and Osterbrock & Dahari (1983), which were taken through a 2.″7 × 4.″0 aperture.

2.3. *VLA Radio Imaging*

Mrk 1066 was observed at 3.6 cm on 1992 December 31 with the NRAO[7] VLA in its A configuration for a total on-source integration time of 17 minutes. Observations were made in two bands, each with 50 MHz bandwidth and separated by 50 MHz. Short observations of 3C 48 and 3C 286 (with adopted flux densities of 3.3 and 5.3 Jy, respectively) were obtained to calibrate the absolute flux density. Observations of the phase reference source, 0248+430, were obtained immediately before and after the observation of Mrk 1066.

To produce the final map, the calibrated visibilities were naturally weighted during the Fourier transform, and the resulting "dirty map" was deconvolved using the CLEAN algorithm. Two iterations of phase-only self-calibration were performed to improve the dynamic range. The deconvolved map has a beam of 0.″26 × 0.″24 (FWHM) with P.A. = −6° and a background rms noise of 0.06 mJy beam^{-1}. This map is very similar to the 6 cm VLA map obtained by Ulvestad & Wilson (1989), which has a resolution of ≃0.″4, and confirms their result that the radio continuum is concentrated into a linear structure in P.A. 134° with length ≈3″. In the 3.6 cm map, a fit to the nuclear radio source with a model including a Gaussian core plus a quadratic background (to represent the extended component) shows that the core source is unresolved. This central component has a flux density of 2.1 ± 0.4 mJy, while the flux density integrated over the linear source is 16.6 ± 0.2 mJy. By comparison, Ulvestad & Wilson (1989) found total flux densities of 35.5 and 94.3 mJy at 6 and 20 cm, respectively.

Superposition of the 3.6 cm and *HST* images adopting their absolute astrometric coordinates reveals an apparent displacement of 0.″4 between the peak of the 3.6 cm map and the peak of the green continuum image. Because such a displacement is typical of the errors in *HST* astrometry and because both the radio and optical continuum images contain a bright peak, we registered the images by aligning these peaks, assuming each peak represents the "true" nucleus. As discussed later (§ 3.2), this assumption is supported by our finding that the continuum peak coincides with the kinematic center.

3. RESULTS

3.1. *Morphology in Continuum and Emission Lines*

Figure 1 contains contour plots of the 5460 Å, 7160 Å, [O III]+Hβ, and Hα+[N II] images, the ratio of the [O III] +Hβ and Hα+[N II] images, and the VLA map at 3.6 cm. Figure 2 (Plate 2) shows the *HST* images (except the 7160 Å image) in gray scale. A narrow "jetlike" feature, extending ≃1.″4 (230 h^{-1} pc) NW of the nucleus, is apparent in the [O III]+Hβ image (Fig. 1*c*). Since this image is dominated by [O III] emission (§ 2.1), we conclude that the high-excitation gas is strongly concentrated in the jet. [O III] emission SE of the nucleus is much fainter than the emission to the NW. The Hα+[N II] image (Fig. 1*d*) also shows the jetlike feature, but the distributon of line emission is broader and more diffuse transverse to the jet axis. The Hα+[N II] emission SE of the nucleus has an intensity only slightly less than that NW of the nucleus (in contrast to the pronounced asymmetry in the [O III] intensity).

At radio frequencies, our 3.6 cm map (Figs. 1*f* and 3), which has better resolution than the maps of Ulvestad & Wilson (1989), shows a central unresolved source surrounded by extended emission which resembles a bipolar jet. The jetlike feature to the NW is quite straight, but the one to the SE widens and curves southward ≃1″ from the nucleus. Both are resolved transverse to their widths. After convolving the [O III] image with a Gaussian to yield the same resolution as the 3.6 cm map, intensity cuts perpendicular to the jet axis show that the NW [O III] jet is narrower than the radio jet.

Although the radio jet is clearly bipolar, the [O III] jet is dominated by the emission NW of the nucleus, with only a trace of line emission associated with the SE radio feature. This apparent asymmetry about the nucleus could result from the [O III] emission SE of the nucleus being seen in projection behind the galactic plane and obscured by dust. A map of the continuum color distribution constructed from the *HST* continuum images does indeed suggest the presence of dust. Figure 4 (Plate 3) presents the distribution of F_λ(7160 Å)/F_λ(5460 Å). Since the effective wavelengths of the F547M and F718M filters are close to those of the Johnson V and R bandpasses, the observed continuum color may be approximately converted to $(V-R)$ by

$$(V-R) \approx 2.5 \log [F_\lambda(7160\ \text{Å})/F_\lambda(5460\ \text{Å})] + 0.85 ,$$

where the zero point is from Allen (1973). Since [S II] emission contributes to the F718M image near the nucleus where there

[7] The National Radio Astronomy Observatory is operated by Associated Universities, Inc., under contract with the National Science Foundation.

PLATE 2

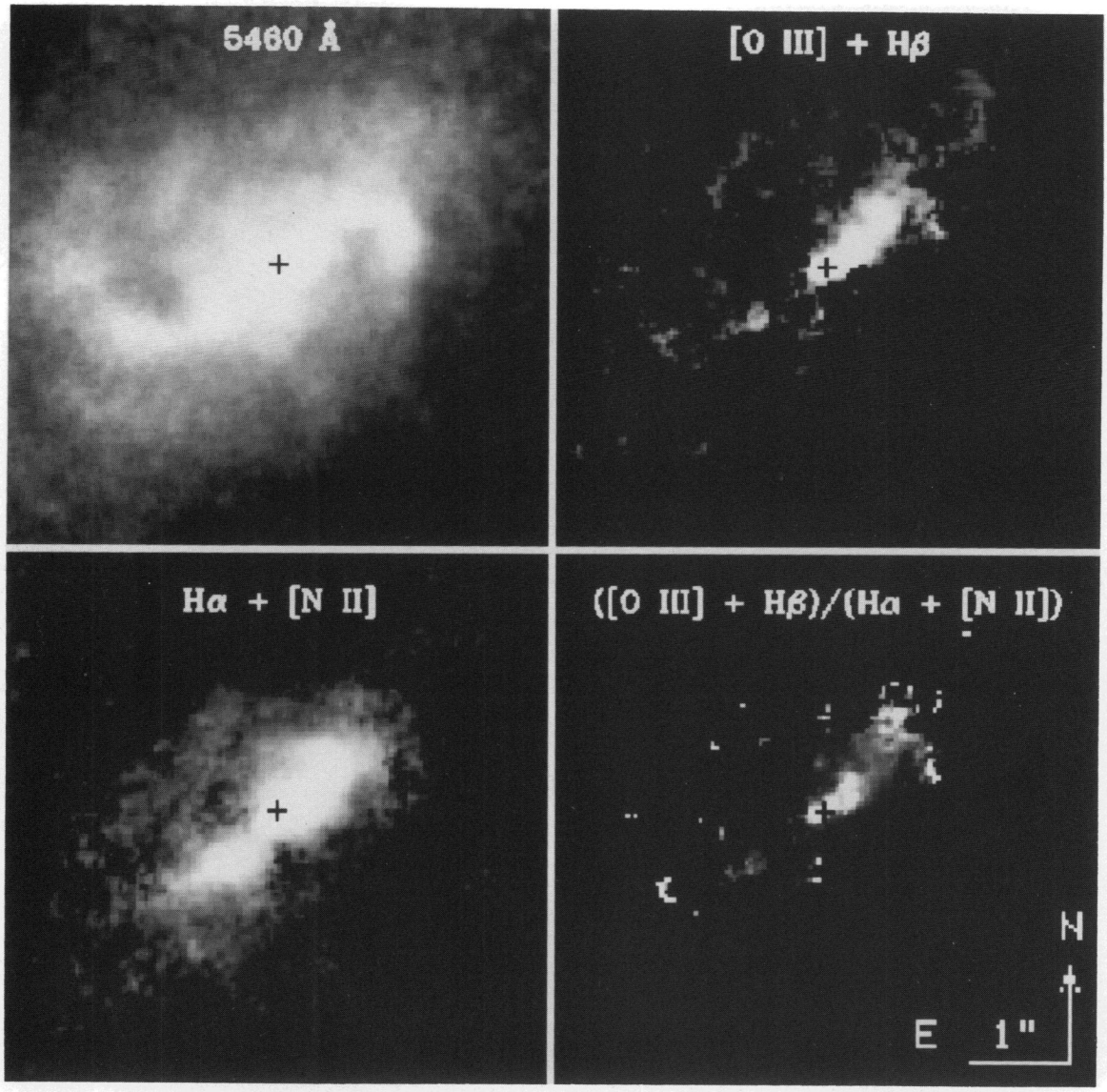

FIG. 2.—Deconvolved *HST* Planetary Camera images (resolution $\simeq 0\farcs1$) of the nuclear region of the type 2 Seyfert galaxy Mrk 1066. The orientation is indicated by the bars, each of which is 1″ long. Intensity scales for the 5460 Å, [O III] + Hβ, and Hα + [N II] images are logarithmic with ranges (with respect to peak intensity) of 0%–15%, 0%–9%, and 0%–15%, respectively. The intensity scale for the ([O III] + Hβ)/(Hα + [N II]) image is linear with values ranging from 0 (*black*) to 1.0 (*white*). A cross marks the position of the nucleus.

BOWER et al. (see 454, 108)

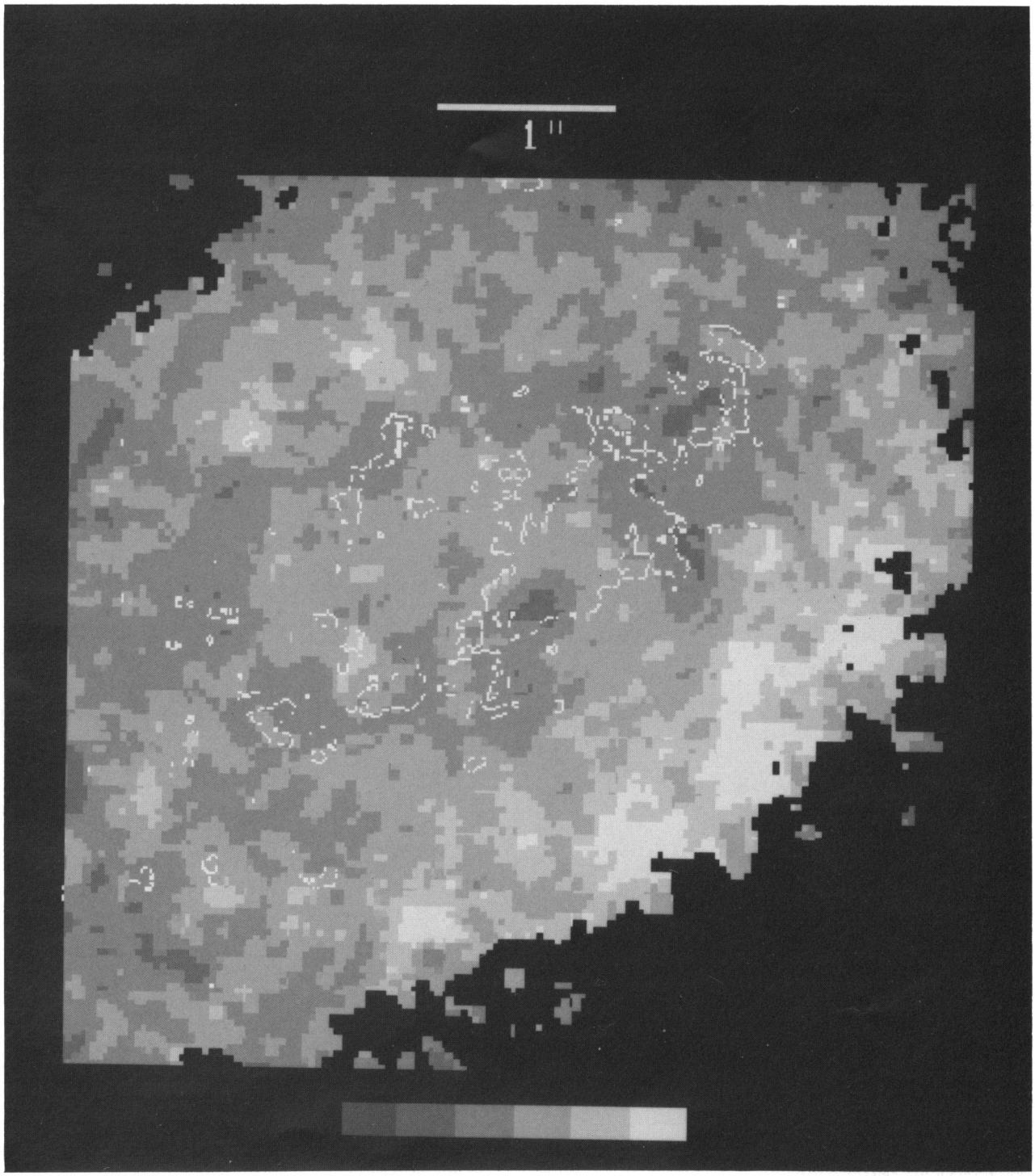

FIG. 4.—A gray-scale map of the *HST* red/green continuum ratio [F_λ(7160 Å)/F_λ(5460 Å)] formed after each image had been convolved with a 3 pixel square median filter, yielding an effective resolution $\approx 0''.3$. North is up, and east to the left. The values of [F_λ(7160 Å)/F_λ(5460 Å)] are binned into the six color bins shown at bottom, which have values of 0.25–2.75 in steps of 0.5. Lighter shades indicate redder continuum colors. In constructing the map, the ratio was set to zero where the continuum surface brightness is less than 5 σ above the background to indicate that the color could not be determined at such locations. All such pixels occur at $R \geq 2''$. The color $(V-R)$ may be obtained from these ratio values by the equation $(V-R) \approx 2.5 \log [F_\lambda(7160\ \text{Å})/F_\lambda(5460\ \text{Å})] + 0.85$. Two contours from the [O III]·+Hβ image (i.e., the lowest and second from highest contour in Fig. 1*c*) are superimposed to provide a reference for locating the [O III] jet and the adopted location of the nucleus.

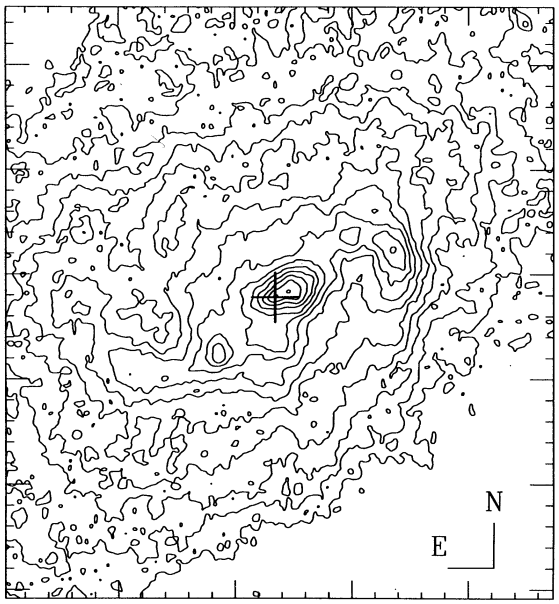

FIG. 1*a*

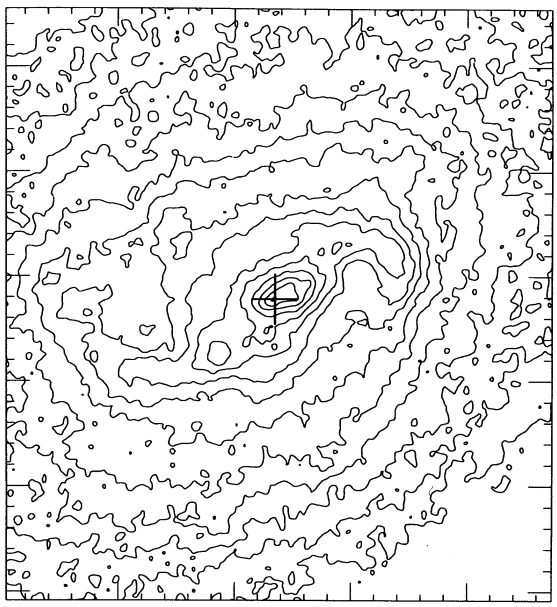

FIG. 1*b*

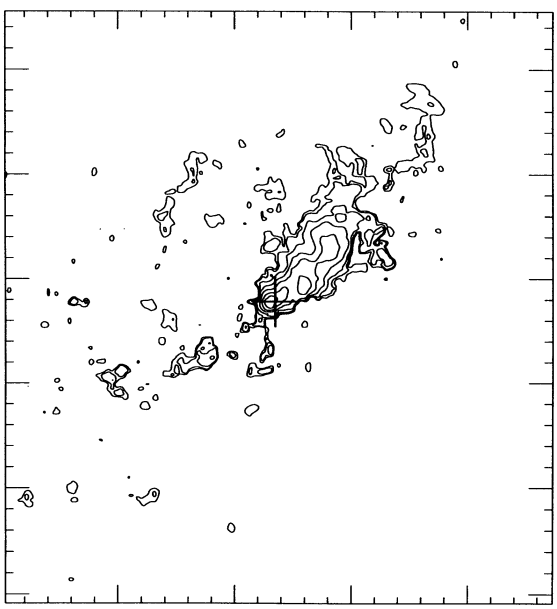

FIG. 1*c*

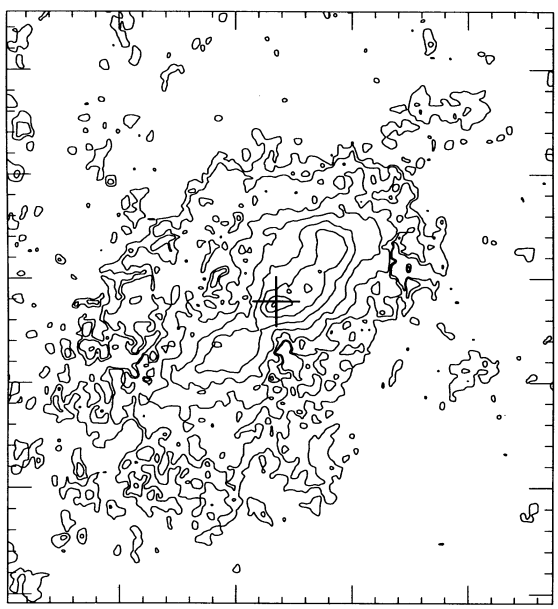

FIG. 1*d*

FIG. 1.—Contour plots of the deconvolved continuum and emission-line *HST* images (*a*–*e*) and the VLA 3.6 cm map (*f*). North is up, and east is to the left. The nucleus is taken to be coincident with the 5460 Å continuum peak and is marked by a cross in all panels. Note that panels (*a*)–(*d*) and (*f*) have identical scales, but the scale is expanded in (*e*). The range of contours includes the peak intensity, except as noted. (*a*) The 5460 Å continuum image; contours range from 1.8×10^{-17} to 7.1×10^{-15} ergs cm^{-2} s^{-1} Å^{-1} arcsec^{-2} with an interval of 0.5 mag. (*b*) The 7160 Å continuum image; contours range from 1.7×10^{-17} to 6.9×10^{-15} ergs cm^{-2} s^{-1} Å^{-1} arcsec^{-2} with an interval of 0.5 mag. (*c*) The [O III] + Hβ image; contours range from 7.2×10^{-15} to 1.8×10^{-12} ergs cm^{-2} s^{-1} arcsec^{-2} (i.e., 40% of peak intensity) with an interval of 1 mag. (*d*) The Hα + [N II] image; contours range from 5.2×10^{-15} to 3.2×10^{-12} ergs cm^{-2} s^{-1} arcsec^{-2} with an interval of 1 mag. (*e*) The ratio of (*c*) to (*d*); the contours correspond to ([O III] + Hβ)/(Hα + [N II]) values of 0.3 through 2.8 (the maximum value) in increments of 0.5. (*f*) The VLA map at 3.6 cm with resolution $\simeq$0″.26. Contours start at 0.1 mJy beam^{-1}, which corresponds to 2 σ, and each contour is 0.5 mag above the previous one. The brightest contour is at 1.58 mJy beam^{-1}, which is 62% of the peak intensity. Mrk 1066 clearly has a linear radio morphology with an unresolved core.

is bright emission-line gas, $(V-R)$ at these locations will be overestimated by $\sim$0.1–0.2 mag (see § 2.1). The observed $(V-R)$ at the nucleus and SE [O III] jet $\approx$0″.9 SE of the nucleus is 1.0 and 1.3, respectively. Although Figure 4 utilizes rather coarse color bins to enhance the color gradient in the nuclear region, the colors given above represent the mean color in the unbinned color map through a circular aperture 0″.3 in diameter. Correcting for Galactic extinction [$A_B = 0.55$, $E(V-R) = 0.12$], yields $(V-R) \approx 0.9$ at the nucleus, and $(V-R) \approx 1.2$ at the SE [O III] jet. Since the observed range of nuclear colors of early-type galaxies is $(V-R) \approx 0.35$–0.8 (Lauberts 1984; Poulain 1988), it seems appropriate to assume

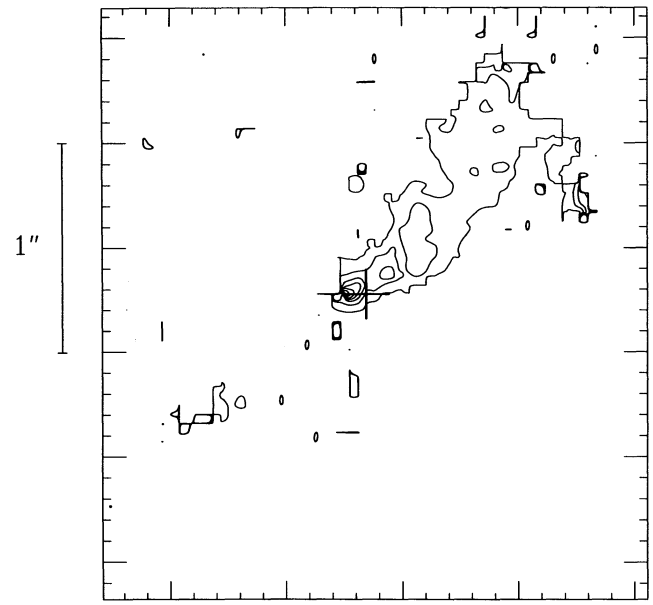

FIG. 1e

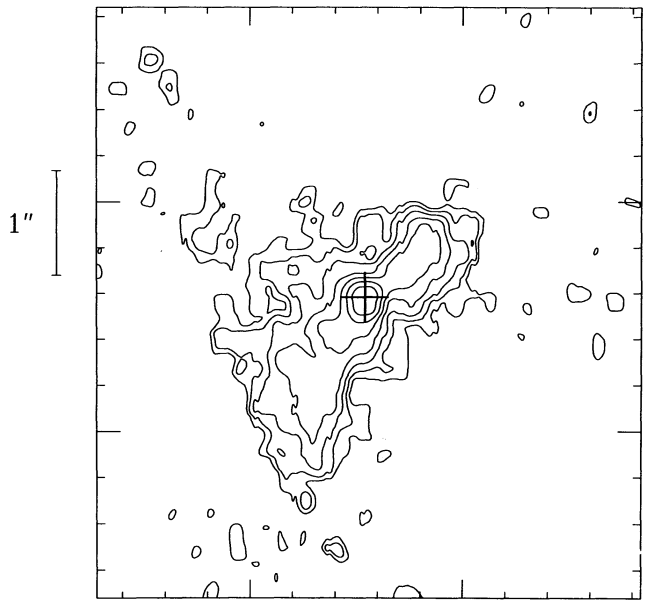

FIG. 1f

that the intrinsic color is ~0.6. For a Galactic extinction curve, this color excess at the SE [O III] jet implies $A_V \approx 2.3$ mag for the stars. Inspection of Figure 1*c* shows that the intensity of [O III] + Hβ emission NW of the nucleus is 20 times brighter than that SE of the nucleus. If these two components have identical intrinsic intensity, then the extinction of the SE [O III] jet at 5007 Å is $A_{5007} = 3.2$ mag, corresponding to $A_V = 2.9$ mag. While the extinctions to disk stars and to gas behind the disk are not expected to be identical, the similarity of these two estimates of A_V renders plausible the notion that the SE jet does emit [O III] but is largely hidden by obscuration. The intensity distribution of Hα + [N II] is much more symmetric about the nucleus, suggesting that much of this emission lies in the galaxy disk. This last conjecture is supported by the kinematics of Hα and [N II] (§ 3.2).

It is notable that both the emission-line gas and the radio emission are approximately aligned with the galaxy's bar (which has P.A. ≈ 143°, see § 1). In the Appendix we examine a well-defined sample of nearby Seyfert galaxies (including Mrk 1066) to determine if there is a relationship between the orientation of bars and that of radio axes in Seyfert nuclei.

3.2. *Kinematics and Excitation*

Figure 5 presents the continuum-subtracted line profiles for the principal emission lines. All profiles have the same velocity scale with the heliocentric velocity of 3625 km s^{-1} plotted as a vertical reference line. Also shown are the slit increment numbers, which are 0.″43 in length, and the position of the peak of the continuum light near Hα (increment No. 0.3). Relative intensity information has been suppressed since all profiles have been scaled to the same height. Figure 6 shows the heliocentric velocity for the center of the profile at 80% peak height (C80) and the profile FWHM, both plotted against distance along the slit. For clarity, a solid line connects the data for Hα while a dotted line connects the data for [O III] λ5007. Fortunately, the origin of the spatial scale was similar for the separate red and green spectra, with continuum light peaks at increment No. 0.3 in the red (adopted in Fig. 7) and increment No. 0.1 in the green. Figure 7 presents the emission-line and continuum fluxes and emission-line flux ratios. Because of the slightly different seeing and nuclear placement on the two nights, we must treat with caution any line ratios which combine red and green lines. For this reason we do not show the Balmer ratio Hα/Hβ, and, in the nuclear region, the ratio [O III] λ5007/Hβ should be considered in preference to the [O III] λ5007/Hα ratio, although this latter ratio should be reliable outside the central 1″–2″ where the flux gradients are less steep.

We consider first the overall rotation curve. The Hα peak velocities trace out what appears to be an approximately symmetric rotation curve (Fig. 6*a*). At $\sim \pm 2''$ the rotation curve turns over at velocities of 3725 ± 5 km s^{-1} (NW) and 3525 ± 10 km s^{-1} (SE). The orientation and amplitude of this rotation curve are consistent with the long-slit spectrum of Veilleux (1991a). However, since Veilleux (1991a) has higher velocity resolution, the rotation gradient over the central 0.″5 in Veilleux's data is larger than our gradient by ~30% (see below). The average of the turnover velocities define a systemic velocity of 3625 ± 12 km s^{-1} which agrees well with the nuclear stellar redshift of 3623 ± 10 km s^{-1} measured from the Ca II triplet (near 8550 Å) and Mg *b* λ5180 spectral regions (Nelson & Whittle 1995). It is interesting that the Na D absorption redshift quoted by Veilleux (1991c) is 3571 km s^{-1} which coincides with the velocity of the peak (i.e., C80) of [O III] λ5007 at the nucleus (see Fig. 6) and is blueshifted by 54 km s^{-1} relative to systemic. Although Veilleux chose the Na D velocity as systemic, we prefer our value of 3625 km s^{-1}, since it relies on gaseous and stellar rotational velocities, and suggest that the Na D absorption is interstellar and participating in the same outflow which is responsible for the blueshifted [O III] λ5007 emission. The full rotation amplitude is 200 ± 12 km s^{-1} or 300 km s^{-1} after correction for an inclination of 42°. This rotation amplitude agrees well with the one given by Afanasiev (1981), although those data only sample length scales beyond ~5″.

The intersection of the systemic velocity with the rotation curve defines a kinematic nuclear position at increment 0.4 ± 0.2, within 0.″1 of the stellar continuum peak. The coin-

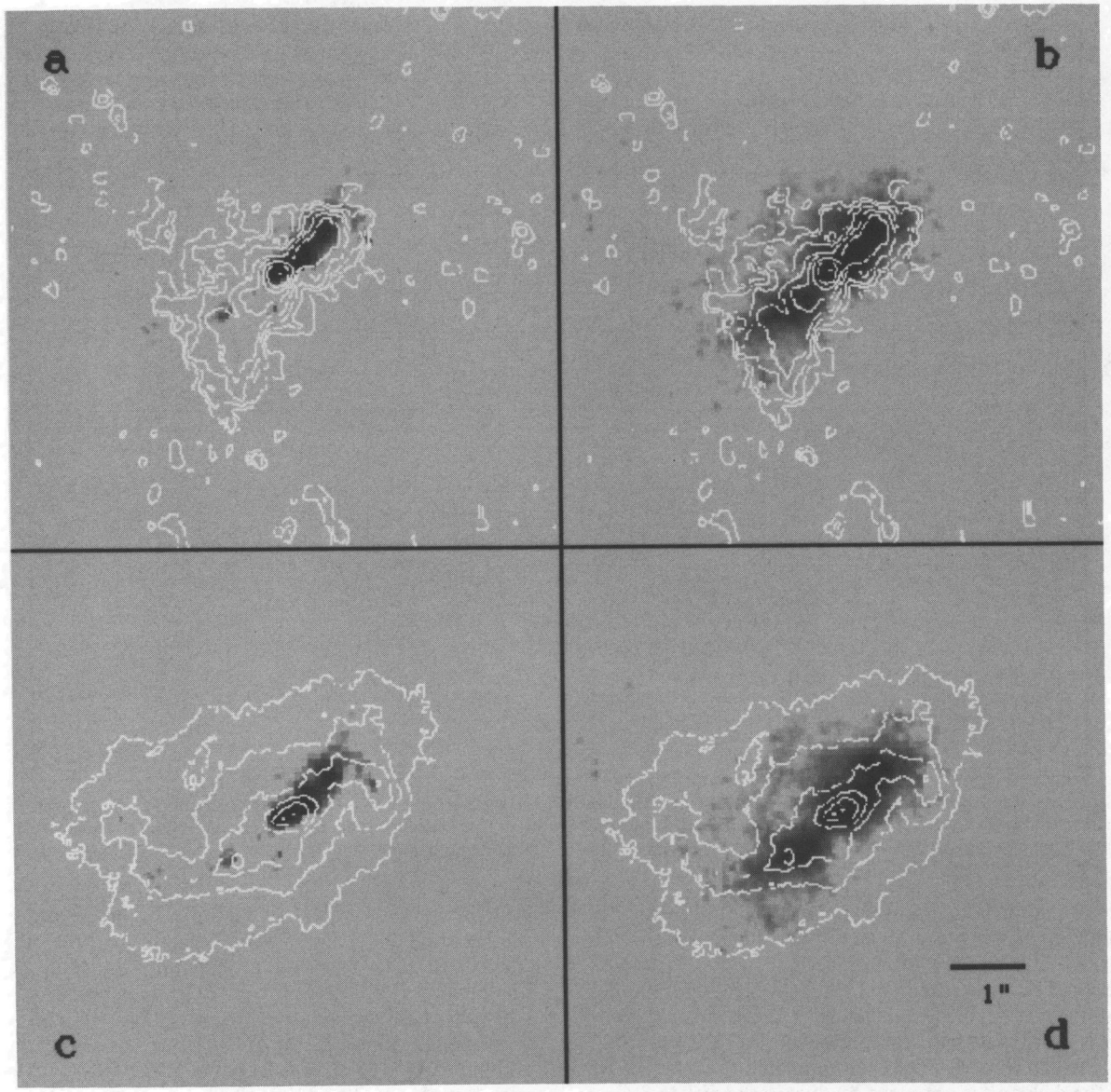

FIG. 3.—The *HST* images displayed using a negative logarithmic stretch with contours from the VLA 3.6 cm and *HST* 5460 Å continuum images superimposed. Panels (*a*) and (*c*) contain the [O III] + Hβ image, while panels (*b*) and (*d*) contain the Hα + [N II] image. Contours from the VLA 3.6 cm map are in panels (*a*) and (*b*), and the 5460 Å continuum contours are in panels (*c*) and (*d*). North is up, and east is to the left. The 3.6 cm contour levels are identical to those in Fig. 1*f*, while the 5460 Å continuum contours start at 7.1×10^{-17} ergs cm^{-2} s^{-1} arcsec^{-2} with an interval of 1 mag. This comparison shows that the emission-line gas in Mrk 1066 is aligned with the 3.6 cm continuum emission.

cidence between the peak of the starlight and the kinematic center (within the limits of these slit data) can also be seen by comparing the Hα profiles from increments 0 and 1 in Figure 5. These profiles show asymmetric shoulders (probably related to the double peak seen by Veilleux (1991a) in the nuclear region) suggesting an inner rotation curve smeared by the seeing. Clearly, the switch from red to blue dominant peaks across these two increments suggests the kinematic center lies somewhere between them. The nuclear velocity gradient is quite steep. A simple estimate using the innermost four C80 values gives 90 km s^{-1} arcsec^{-1} or 550 h km s^{-1} kpc^{-1}. However, the true nuclear gradient is much steeper. Using the two peak velocities from increments 0 and 1, we find a lower limit of $\sim$195 km s^{-1} arcsec^{-1} or 1.2×10^3 h km s^{-1} kpc^{-1} ($\sim 1.8 \times 10^3$ h km s^{-1} kpc^{-1} deprojected). Veilleux (1991a) found that the two Hα-emitting components separated by $\sim$0.″5 have a velocity difference of $\Delta V = 125 \pm 20$ km s^{-1}, implying a rotation gradient of 250 km s^{-1} arcsec^{-1} or 1.5×10^3 h km s^{-1} kpc^{-1}. The steep rotation curve does not, however, imply an unusually high mass-to-light ratio. Taking our rotation at $\pm 2''$ to estimate the mass, and the continuum flux to estimate the light, we derive $M/L_B \sim$ (2–4) h.

Determining the orientation of the disk requires knowing the sense of rotation. Although de Vaucouleurs et al. (1991) classify Mrk 1066 as (R)SB(s)0$^+$, the outer features visible on the Palomar Observatory Sky Survey plate could be interpreted as spiral arms rather than an outer ring. In the *HST* continuum images (e.g., Fig. 1*a*), inner spiral arms are apparent

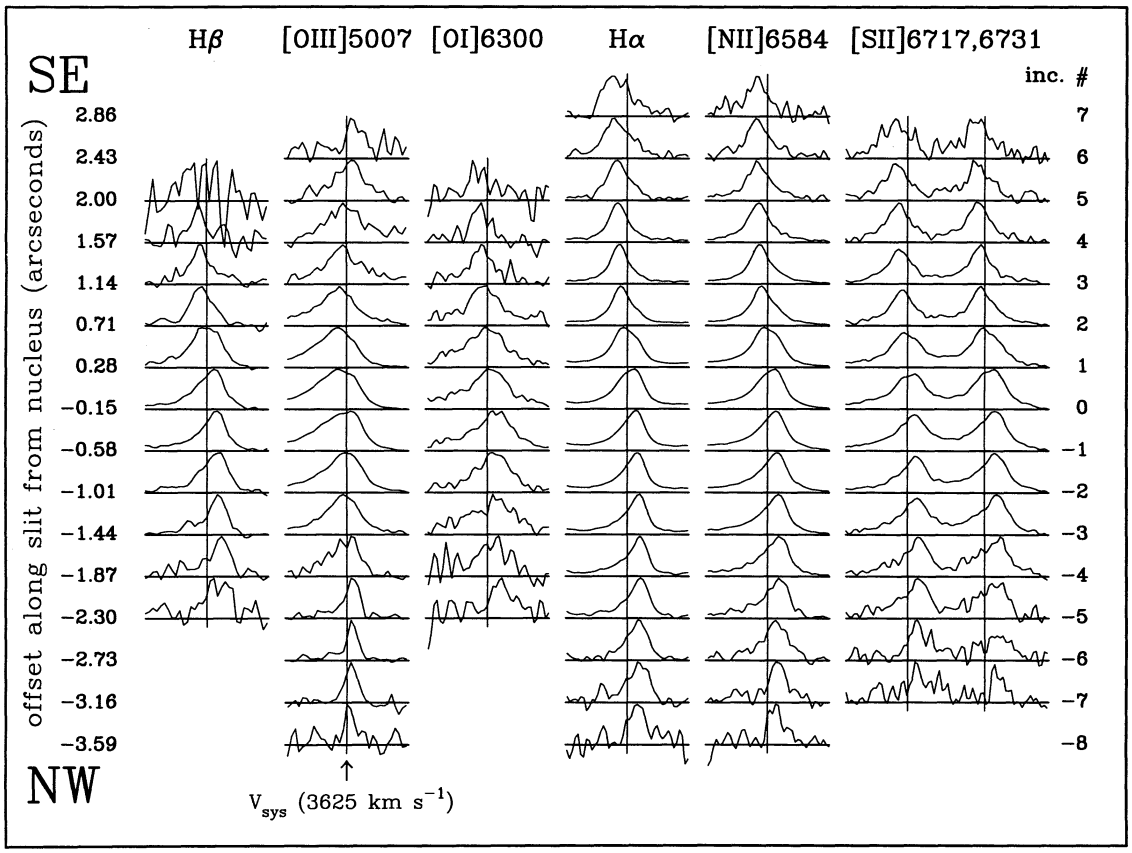

FIG. 5.—Sequences of emission-line profiles along P.A. = 134° at 0.″43 intervals, for Hβ, [O III] λ5007, [O I] λ6300, Hα, [N II] λ6584, and [S II] λλ6717, 6731. Each plot has the same velocity scale; the total range plotted is 1000 km s^{-1} (except for the [S II] profiles). Vertical lines correspond to the systemic velocity of 3625 km s^{-1}. Spatial pixel numbers are given on the right, and the offset from the continuum nucleus in arcseconds is on the left.

within ≈2″ of the nucleus. Assuming that the spiral arms trail the rotation, the galaxy rotates in a counter-clockwise sense on the sky. If the major axis position angle is indeed 90° (see § 1), then the sense of the measured rotation curve (Fig. 6*a*) implies that the south side of the galaxy disk is the near side. This orientation is consistent with the presence of a dust band 1.″5 SW of the nucleus (Fig. 4). It is then plausible that the SE jet lies behind the disk and is obscured by dust in the disk (§ 3.1).

Turning to the luminosity distributions, our slit spectra are generally consistent with the *HST* images. In particular, in the long-slit spectra the peaks in the emission-line distributions lie ~0.6–1.0 increments (~0.″25–0.″43) to the NW of the stellar peak, with marginal evidence that [O I] is slightly more offset than Hα and Hβ (Fig. 7*a*). In the absence of kinematic information, it would be difficult to decide whether the true nucleus fell at the emission-line peak or the starlight peak. However, since the kinematic center coincides with the starlight peak, the true nucleus and the emission-line distributions seem to be genuinely offset. This offset between the continuum and emission-line peaks is in excellent agreement with the *HST* images (§ 3.1). From these images, it is apparent that the [O III] emission-line gas is concentrated into a "jetlike" structure with the continuum peak near its base. Convolving the *HST* images with Gaussians to yield an effective resolution of 1″ shows that the peaks in both [O III] + Hβ and Hα + [N II] are 0.″22 NW of the continuum peak.

Perhaps the most striking properties of the line profiles and ratios are those which point to the presence of more than one ionization component. For example, Figures 5 and 6 show that the Hα and [O III] λ5007 velocity fields are quite different, with the [O III] line showing little if any rotation. To the NW (increments −8 to −5) the [O III] line is narrower and somewhat blueshifted relative to Hα. Across the central 2″ (increments −2 to 2), the [O III] line is significantly broader and blueshifted relative to Hα, and it also has an extended blue wing (see also Veilleux 1991a). The maximum [O III] line width occurs at increment −1, close to the peak line intensity, while the maximum Hα line width occurs at the stellar and kinematic nucleus, where the smeared rotation curve causes an apparent line broadening. To the SE, Hα traces out the blue part of the rotation curve while [O III] shifts in velocity to the red, so that [O III] and Hα are on *opposite* sides of the systemic velocity beyond 1.″5 from the nucleus. It is interesting that the other lines show behavior intermediate between [O III] and Hα. For example, while the peak velocities of [N II] λ6584 and [O I] λ6300 follow Hα reasonably well, their line widths are significantly greater across the nuclear regions, with [O I] (and possibly [N II]) line widths intermediate between [O III] and Hα. On the nucleus, this behavior is typical of many Seyfert galaxies which can show a range of line widths for different emission lines. Here, however, these differences are traced over an extended region. Clearly, the slit includes emission from gas with a range of both ionization conditions and velocity fields.

We may use line ratios to try to identify these ionization components in more detail. From their single aperture data, Osterbrock & Dahari (1983) consider Mrk 1066 to be a

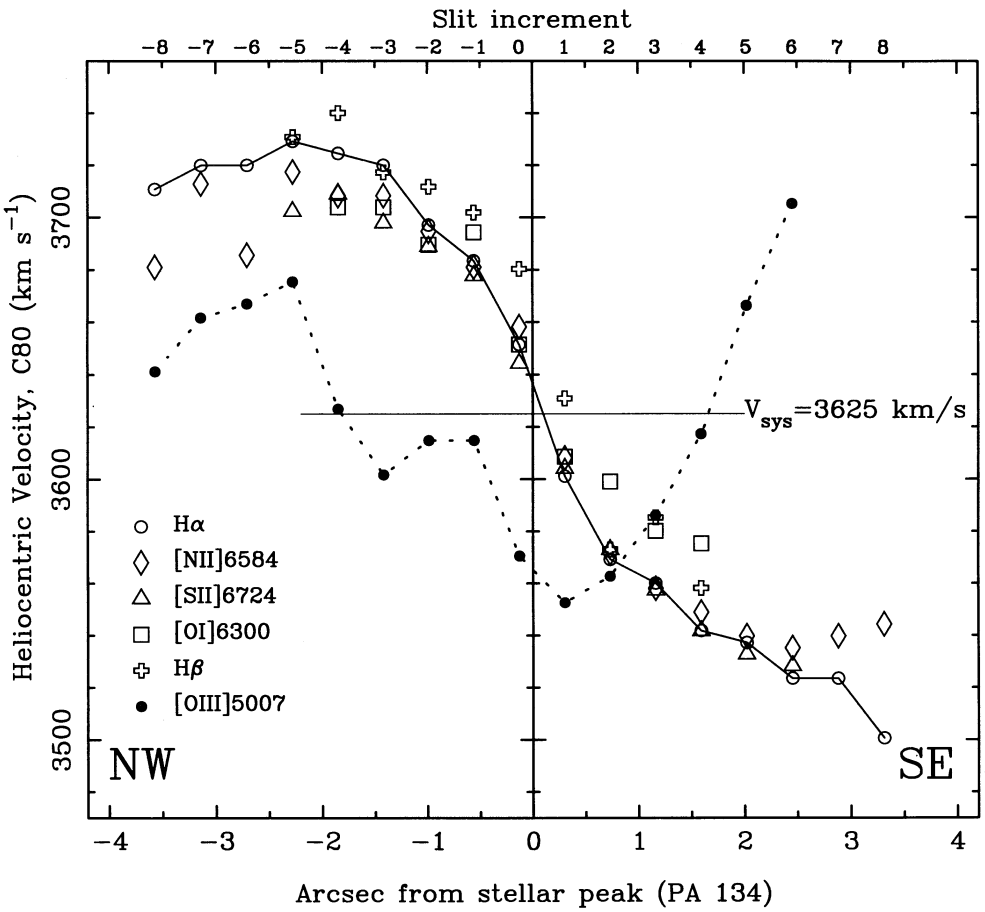

FIG. 6*a*

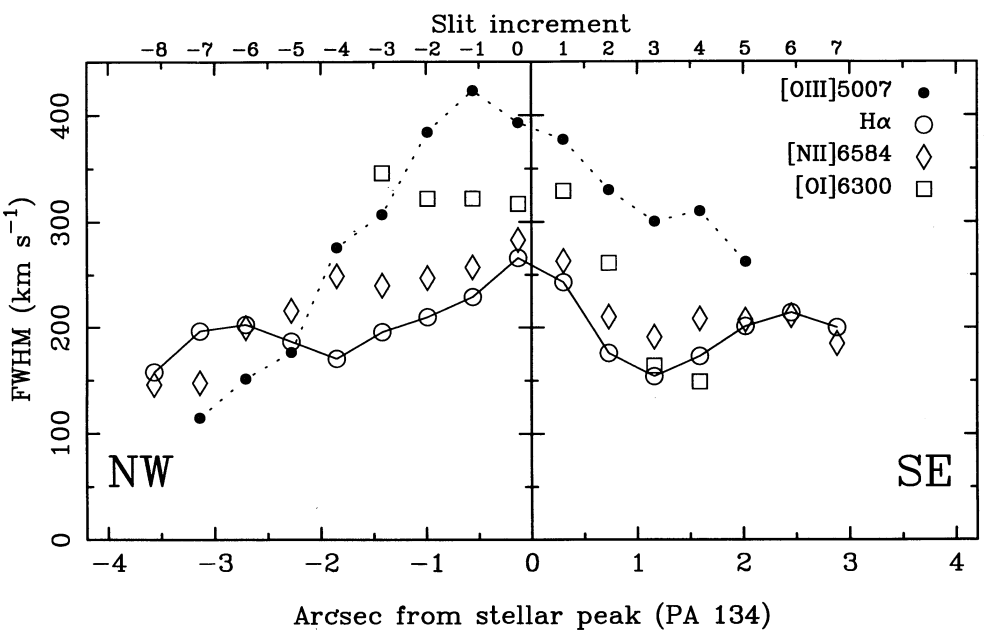

FIG. 6*b*

FIG. 6.—(*a*) Heliocentric velocity for C80 (the center of the profile at 80% peak height) in km s^{-1} for the principal emission lines. (*b*) Profile FWHM in km s^{-1}. In both plots, a solid line connects the Hα data and a dotted line connects the [O III] λ5007 data. Symbol keys are given on the plot. The spatial scale is given in arcseconds relative to the continuum nucleus (*lower axis*) and relative pixel number (*top axis*).

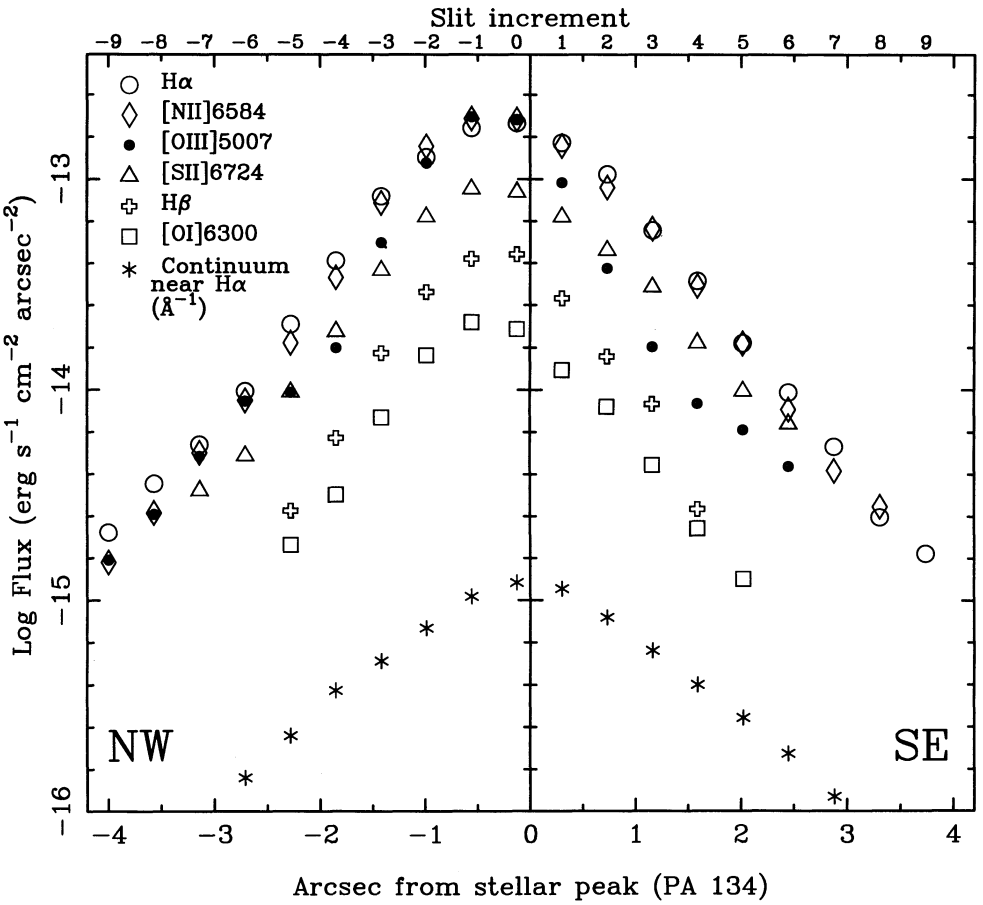

FIG. 7*a*

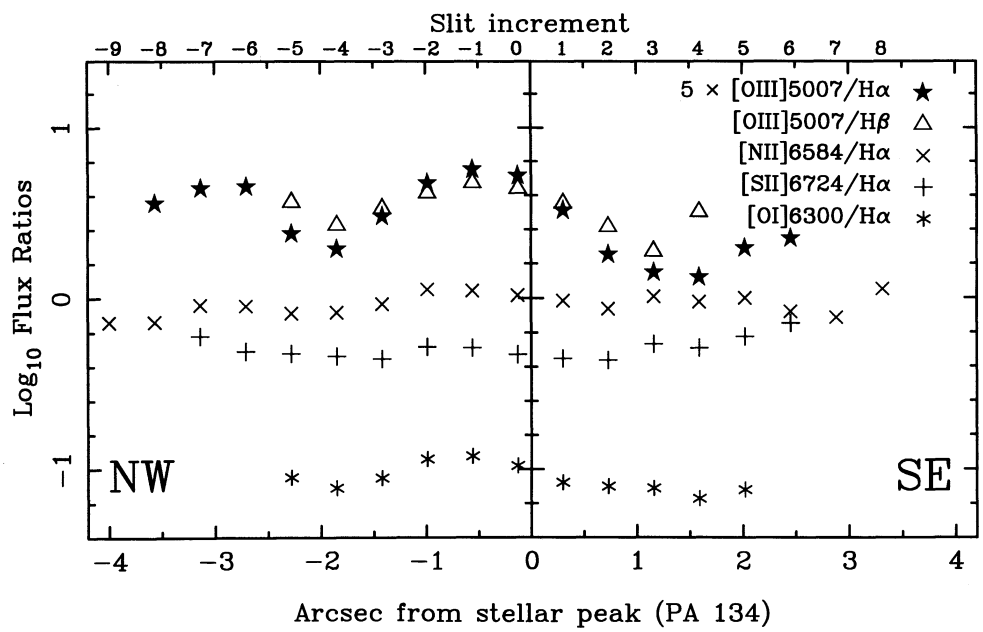

FIG. 7*b*

FIG. 7.—(*a*) Integrated line fluxes in ergs s^{-1} cm^{-2} $arcsec^{-2}$ for each emission line. The continuum emission is also shown, in ergs s^{-1} cm^{-2} $Å^{-1}$ $arcsec^{-2}$. (*b*) Line flux ratios derived from the same data. Note that the [O III] λ5007/Hα ratio has been multiplied by a factor of 5 for clarity. Symbol keys are given on the plot. The spatial scale is given in arcseconds relative to the continuum nucleus (*lower axis*) and relative pixel number (*top axis*).

"marginal" Seyfert 2, since a value for [O III] λ5007/Hβ of $\sim$4 is barely above the threshold for Seyfert galaxies, while [O I] λ6300, [N II] λ6584, and [O II] λ3727 are not sufficiently strong to qualify as a LINER, although they do suggest the emission is not from normal H II regions. In our long-slit data, we see these ratios change along the slit (Fig. 7*b*). At the emission-line peak (increment number of roughly -1) the line ratios are intermediate between those of a Seyfert galaxy and a LINER, though somewhat higher excitation than the single-aperture data. Away from this peak, the [O III] λ5007/Hβ ratio drops by a factor $\sim$2 out to $\pm 1\farcs5$, while the [O I] λ6300, [N II] λ6584, and [S II] $\lambda\lambda$6717, 6731 lines get slightly weaker relative to Hα (note that the [O III] λ5007/Hα drop shown in Figure 7*b* is higher than that of [O III] λ5007/Hβ, probably because of either the slight difference in seeing between the two nights or variations in reddening of the emission-line gas). Beyond this minimum, these line ratios reverse, and outside $\sim 2''$ the [O III] λ5007 line has recovered strength relative to the Balmer lines suggesting the gas is once again of relatively high excitation. Interpreting these line ratio changes in terms of differing proportions of Seyfert and LINER emission is not, however, straightforward. For example, although the near nuclear decrease in [O III] λ5007/Hβ suggests a move toward LINER conditions, the decrease in [O I] λ6300/Hα represents a move away from LINER conditions. Similarly, the subsequent reversal in excitation does not clearly move toward Seyfert conditions, since ([S II] λ6717 + λ6731)/Hα and [O I] λ6300/Hα also appear to increase. Although these line ratio changes alert us to changing ionization conditions, they are not very useful at deciphering them, as might be accomplished by plotting line ratios at different positions in diagnostic diagrams (e.g., Veilleux & Osterbrock 1987). This is not too surprising since the line *profiles* are so different, and integrated flux ratios still average over all velocities. If, instead, profile ratios are formed, then a much larger range in excitation becomes apparent, with the blueshifted gas having [O III] λ5007/H$\beta \sim$ 10–15 while the normally rotating gas has [O III] λ5007/H$\beta \sim$ 2–3. Since the [O I] λ6300 line appears to share the overall rotation of the Balmer lines, we conclude that the rotating low-excitation component is indeed LINER-like while the nuclear blueshifted and off-nuclear redshifted gas traced by [O III] λ5007 is higher excitation Seyfert-like emission. Thus the observed emission-line ratio at a given position would depend on the relative brightnesses of these two components. The most natural explanation for the difference in velocity field is that the high-excitation component (which might be exposed more directly to the nuclear ionizing radiation) is in outflow and the low-excitation component lies in the galactic disk. Thus, the kinematics and excitation of the two gaseous components are broadly consistent with the idea suggested in § 3.1 in which the high-excitation gas is inclined with respect to the disk and the low-excitation gas lies in the plane of the disk. However, a few details of the kinematics imply a more complicated situation. Although the rotation curve for [O I] (Fig. 6*a*) shows rotation about the nucleus (similar to other low-excitation lines), the FWHM of [O I] is typically much greater than that of Hα (see Fig. 6*b*).

4. DISCUSSION

Section 3 discussed the two components of circumnuclear ionized gas in Mrk 1066, including a diffuse, low-excitation LINER-like component whose kinematics follow a normal rotation curve, and a collimated, high-excitation Seyfert-like component showing anomalous kinematics (possibly indicating a bipolar outflow). Many other Seyfert galaxies with both high- and low-excitation emission-line components have been identified previously. The kinematics of the high-excitation gas in these galaxies are often consistent with radial outflow from the nucleus (e.g., Phillips et al. 1983; Wilson et al. 1986; Storchi-Bergmann, Wilson, & Baldwin 1992). In this section, we provide a preliminary investigation of possible ionization sources.

Photoionization is commonly believed to be the excitation mechanism for the emission lines in Seyfert galaxies. However, in cases where there are multiple kinematic components with very different excitation properties, investigators have identified more than one source of ionizing photons. For example, in the type 1 Seyfert galaxy NGC 7469, Wilson et al. (1986, 1991) concluded that the high-excitation gas near the nucleus is photoionized by a compact ionizing source with a relatively hard spectrum, while the low-excitation extended gas is photoionized by hot stars in a circumnuclear starburst ring. Similarly, in the type 2 Seyfert galaxy NGC 7582, Morris et al. (1985) found that the Hα emission is primarily confined to the galactic disk, but the higher excitation [O III] emission emanates from an outflowing wind. It is important to note, however, that the low-excitation emission-line ratios in these two examples are characteristic of normal H II regions; the low-excitation line ratios in Mrk 1066 are LINER-like, for which case hot stars are probably not the ionizing source (Ho, Filippenko, & Sargent 1993).

We can use the spatial and kinematic segregation of the high- and low-excitation emission components in Mrk 1066 to help identify the sources of ionizing photons. The degree of excitation is related to the ionization parameter $U = Q(H^0)/4\pi r^2 c N_e$, where $Q(H^0)$ is the rate at which ionizing photons are emitted from a point source toward a gas cloud with electron density N_e and distance r from the ionizing source. The value of U in Seyfert-excited gas exceeds that in LINERs by a factor of $\sim$10 (e.g., Ho et al. 1993). Variations in U require that $Q(H^0)$, r, and/or N_e are different on the high- and low-excitation emission regions. If the nucleus of Mrk 1066 is the only source of ionizing radiation, the difference in U does not appear to be solely due to differences in r, because the collimated Seyfert-like gas and the more diffuse LINER gas lie at nearly identical projected distances from the central source. Further, the high-excitation "jet" appears relatively bright, not only in [O III] but also in Hα + [N II] (Fig. 2). The jet's higher emissivity suggests that N_e is higher in the Seyfert-like gas than in the low-excitation gas, which would change the value of U in the opposite direction to that observed. Consequently, the variation in U seems to require that $Q(H^0)$ seen by the jet is much larger than that seen by the LINER gas. Two scenarios in which the jet would be illuminated by a much higher flux of ionizing photons than the LINER gas are (1) the ionizing photons are emitted anisotropically from the central source, being beamed preferentially along the jet and (2) the ionizing photons are created *in situ* by the jet itself.

Anisotropic emission of ionizing photons could arise if the nuclear source is surrounded by a torus of gas and dust, the plane of which is oriented perpendicular to the radio axis. There is considerable evidence for such tori in many types of AGNs, especially Seyfert 2 galaxies (Antonucci 1993). Although the detection of broad permitted emission lines in polarized light can provide strong evidence for a blocking torus in type 2 Seyfert galaxies (e.g., Tran, Miller, & Kay 1992),

spectropolarimetry of Mrk 1066 does not reveal any such broad lines (Miller & Goodrich 1990; Kay 1994; Hurt 1994). The continuum polarization in the UV (where starlight in the host galaxy and interstellar polarization are less significant than in the optical) is only $1.7 \pm 0.9\%$ and has position angle $= 137 \pm 15°$ (Hurt 1994), which is *parallel* to the radio axis, unlike the perpendicular polarization seen in Seyfert 2 galaxies with scattered nuclear light.

In high-resolution imaging, a possible signature of a torus is a compact region of excess reddening and/or obscuration at the nucleus. For example, Mulchaey et al. (1994) detected an unresolved region of excess reddening at the nucleus of the type 2 Seyfert NGC 2110. In the color map of Mrk 1066 (Fig. 4), the nucleus is actually bluer than regions $\geq 0\farcs5$ away, and its color is typical of an early-type galaxy. We conclude that there is no direct evidence for an obscuring torus with size $\geq 16\ h^{-1}$ pc around the nucleus of Mrk 1066.

The close spatial association between the radio jet and the collimated, high-excitation optical emission, together with the anomalous velocity field of the high-excitation gas, indicates an interaction between the radio jet and the circumnuclear gas. Shocks, which can accelerate and excite ambient interstellar clouds, may form along the boundary of the jet. UV and X-ray photons are emitted from the hot regions behind these shocks and may photoionize both the ambient surroundings and the postshock gas. Sutherland, Bicknell, & Dopita (1993) have presented models for the interaction of the radio jet in Centaurus A with dense clouds. Using shock velocities of ~ 300–450 km s^{-1}, their models predict [O III] $\lambda 5007/\mathrm{H}\beta$ line ratios ≥ 10, similar to the values we observe for the high-excitation component in Mrk 1066. The qualitative appeal of the Sutherland et al. (1993) models in the context of Mrk 1066 is that they are built upon plausible assumptions about the interaction of the radio jet with its surroundings, do not require a highly beamed ionizing radiation field from the nucleus, and naturally give rise to a component of gas with anomalous kinematics relative to the galactic rotation curve. Unfortunately, our data are too limited to derive a complete set of emission-line diagnostics in the high-excitation gas for comparison with the shock models. The decrease in excitation (as measured by the $([\mathrm{O\ III}] + \mathrm{H}\beta)/(\mathrm{H}\alpha + [\mathrm{N\ II}])$ ratio; see Fig. 2) away from the nucleus along the jet is suggestive of a decrease in average shock velocity, but is also expected in central source photoionization models.

5. SUMMARY

We have analyzed high-resolution optical and radio images and optical spectroscopy of the type 2 Seyfert galaxy Mrk 1066. The morphology, kinematics, and excitation of the emission-line gas and its relationship to the radio continuum source may be summarized as follows:

1. The distributions of emission-line gas and radio continuum are consistent with a bipolar jet inclined significantly to the galactic disk. A narrow "jetlike" feature, extending $1\farcs4$ ($230\ h^{-1}$ pc) NW of the nucleus, is apparent in the distribution of high-excitation gas (as delineated by [O III]). The $\mathrm{H}\alpha + [\mathrm{N\ II}]$ emission is aligned with the [O III] emission, but is less strongly concentrated into a jet. Thus the spatial distributions of the low- and high-excitation gases are different. In contrast to the one-sided [O III] emission, the 3.6 cm radio continuum map exhibits a bipolar jet.

2. These high- and low-excitation emission-line components are kinematically distinct: the [O III]-emitting gas exhibits peculiar kinematics with respect to the rotation curve traced by the low-excitation emission lines. Relative to this rotation curve, the [O III]-emitting gas is blueshifted NW of the nucleus and redshifted SE of the nucleus. The kinematics of the high-excitation gas probably reflect outflow driven by the radio jet.

3. Assuming that spatial variations in the intrinsic optical continuum color are insignificant, the extinction is found to vary significantly with position over the galactic disk. A map of the continuum color shows that the nucleus has extinction $A_V \approx 1.2$ mag, while the location $\approx 80\ h^{-1}$ pc SE of it along the jet axis has extinction $A_V \approx 2.3$ mag. An extinction of this order of magnitude is sufficent to hide most of the [O III] emission of the SE jet if this feature is on the far side of the galactic disk and has a similar intrinsic brightness in [O III] as the NW jet. Since the low-excitation gas probably lies in the galactic plane (as indicated by its rotational kinematics), the $\mathrm{H}\alpha + [\mathrm{N\ II}]$ emission is more symmetrically disposed about the nucleus.

4. Two possible scenarios can account for the concentration of high-excitation gas in a jet and LINER-like gas in the galactic plane: (*a*) the ionizing photons are emitted anisotropically from a central source and are beamed preferentially along the jet or (*b*) ionizing photons are created *in situ* in shocks formed at the boundary between the jet and ambient cloud material. The former scenario would arise naturally if the central source is surrounded by a dusty torus; however, there is currently no convincing evidence for such a torus in Mrk 1066. Useful constraints on the latter scenario might be provided by improved spectroscopy to determine accurately the line ratios for each emission-line component.

We thank L. Bergeron for assistance with the reduction of the *HST* images and J. Gallimore for reducing the VLA 3.6 cm observations. We acknowledge useful discussions with the anonymous referee and with T. Hurt, A. Koekemoer, J. Krolik, and T. Storchi-Bergmann, S. Westphal assisted with the plates. Partial support for this work was provided by NASA through grant number GO-3724 from the Space Telescope Science Institute, which is operated by AURA, Inc., under NASA contract NAS5-26555. Additional support was provided by NASA grants NAGW-2689 and NAGW-3268. J. S. M. acknowledges support from a STScI graduate student fellowship.

APPENDIX A

We examine the relationship between linear radio sources and bars in Seyfert galaxies to determine if the apparent alignment seen in Mrk 1066 is common among Seyfert galaxies. Bars in Seyfert galaxies might play a key role in the transportation of gas toward the nucleus (e.g., Simkin, Su, & Schwarz 1980; Shlosman, Frank, & Begelman 1989). However, it is also apparent that gas probably can be transported by other means since there is no statistically significant excess of bars among Seyfert galaxies when compared to non-Seyfert galaxies (e.g., Heckman 1978; Simkin et al. 1980). The nuclear gas may settle preferentially into a disk with rotation axis parallel to the bar (Durisen et al. 1983; Tohline & Osterbrock 1982). This gas disk could then collimate the emission of ionizing

TABLE 2

LINEAR RADIO SOURCES IN BARRED SEYFERT GALAXIES

GALAXY (1)	MORPHOLOGICAL TYPE (2)	SEYFERT TYPE (3)	P.A. radio (4)	P.A. bar (5)	P.A. major (6)	REFERENCE (7)
NGC 591 = Mrk 1157	(R′)SB0/a	2	152°	92°:	5°	1
NGC 2273 = Mrk 620	SB(r)a	2	90	129	50	2
NGC 4051	SAB(rs)bc	1.5	81	156	135	3
NGC 4151	(R′)SAB(rs)ab	1.5	92	132	26	4
NGC 5643	SAB(rs)c	2	87	90	128	5
NGC 7450 = Mrk 1126	(R)SB(r)a	1.5	100	28	35	6
Mrk 1066	(R)SB(s)0$^+$	2	135	143	90:	7
0714−2914 = MCG − 5-18-2	SAB(r)0^0 pec	2	129	124	140	8

REFERENCES.—(1) Haniff et al. 1988; (2) van Driel & Buta 1991; (3) Wray 1988; (4) Arp 1977; (5) Morris et al. 1985; (6) Mazzarella & Boroson 1993; (7) this paper; (8) Wilson & Baldwin 1989.

photons from the central source as well as the ejection of hot plasma along the bar's major axis. Morris et al. (1985) present a schematic diagram of this model in their investigation of NGC 5643, a type 2 Seyfert galaxy in which the axes of the bar and linear radio source are aligned. Analysis of a well-defined sample of Seyfert galaxies would determine if this scenario might apply to other Seyfert nuclei.

A survey of all Seyfert galaxies identified as of mid-1983 with $\delta \geq -45°$ and redshifts with respect to the centroid of the Local Group less than 4600 km s^{-1} was completed by Ulvestad & Wilson (1984, 1989) by obtaining high-resolution radio continuum maps with the VLA. They divided the radio morphologies into five different types: unresolved, slightly resolved, diffuse, linear (i.e., double, triple, or jetlike), or ambiguous. Table 2 lists all Seyfert galaxies with linear radio sources found by Ulvestad & Wilson in host galaxies classifed as barred in optical images. Also listed are the morphological type (from de Vaucouleurs et al. 1991), Seyfert type, and the position angles of the radio axis, bar, and photometric major axis. Although NGC 2110 is classified as SAB0$^-$, there is no evidence of a bar in images of this galaxy (Wilson, Baldwin, & Ulvestad 1985; Mulchaey et al. 1994), so it is not included in Table 2. Of the eight galaxies, the bar in NGC 591 is not very prominent. The position angles of the bars were measured on scales of $\sim$1 kpc (from the references given in [7]), while those of the linear radio sources apply to the central $\sim$100–200 pc. Major axis position angles were adopted from de Vaucouleurs et al. (1991) or Nilson (1973). Uncertain measurements are flagged by a colon; errors in the remaining values are as high as $\pm 10°$. Figure 8 (which shows the distribution of the offset between the radio axes and bars)

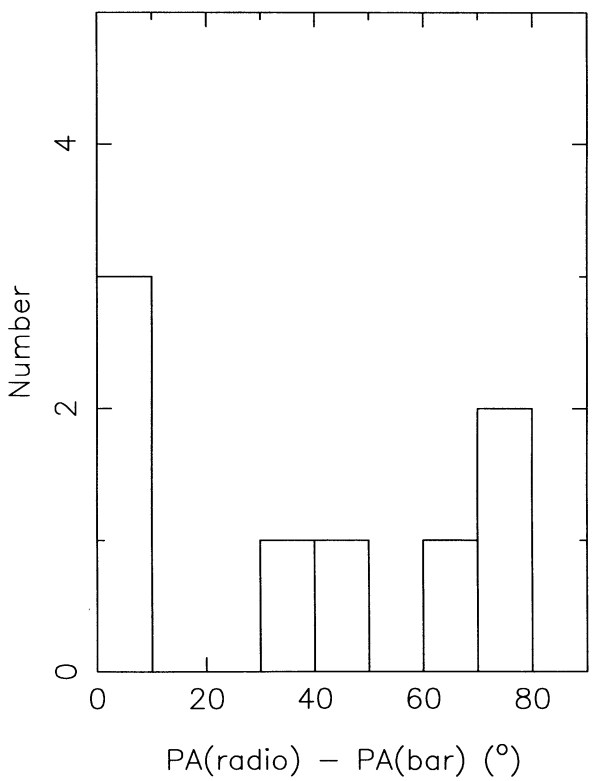

FIG. 8.—The distribution of the offset between the radio axis and bar major axis for the galaxies in Table 2. If the position angle of the bar is not preferentially aligned with the radio axis, one would expect a uniform distribution.

demonstrates that, despite a statistically insignificant excess at zero offset, there is no significant relationship between the orientation of the bar and the radio axis in Seyfert galaxies. This result is not significantly affected if NGC 1068 were to be included in the sample. Although NGC 1068 is classified as SA, it has a prominent bar with P.A. $\approx 48°$ in K-band images (Scoville et al. 1988) and a linear radio source with P.A. $\approx 28°$ (Wilson & Ulvestad 1983). The lack of a trend in Figure 8 is consistent with our picture of Mrk 1066, in which the radio jets are oriented out of the galaxy disk and only appear to align with the bar through projection.

REFERENCES

Afanasiev, V. L. 1981, Soviet Astron. Lett., 7, 215
Allen, C. W. 1973, Astrophysical Quantities (London: Athlone)
Antonucci, R. 1993, ARA&A, 31, 473
Arp, H. 1977, ApJ, 218, 70
Bower, G. A., Wilson, A. S., Mulchaey, J. S., Miley, G. K., Heckman, T. M., & Krolik, J. H. 1994, AJ, 107, 1686
Cecil, G. 1988, ApJ, 329, 38
Cecil, G., Bland, J., & Tully, R. B. 1990, ApJ, 355, 70
de Vaucouleurs, G., de Vaucouleurs, A., Corwin, H. G., Buta, R. J., Paturel, G., & Foque, P. 1991, Third Reference Catalog of Bright Galaxies (New York: Springer)
Durisen, R. H., Tohline, J. E., Burns, J. A., & Dobrovolskis, A. R. 1983, ApJ, 264, 392
Goodrich, R. W., & Osterbrock, D. E. 1983, ApJ, 269, 416
Haniff, C. A., Wilson, A. S., & Ward, M. J. 1988, ApJ, 334, 104
Heckman, T. M. 1978, PASP, 90, 241
Ho, L. C., Filippenko, A. V., & Sargent, W. L. W. 1993, ApJ, 417, 63
Hurt, T. 1994, in Proc. Oxford Astrophysics Workshop on "Evidence for the Torus," ed. M. J. Ward (Oxford: Oxford Univ. Press), 129
Kay, L. E. 1994, ApJ, 430, 196
Lauberts, A. 1984, A&AS, 58, 249
Lucy, L. B. 1974, AJ, 79, 745
MacKenty, J. W., et al. 1992, *Hubble Space Telescope* Wide Field and Planetary Camera Instrument Handbook, Version 3.0 (Baltimore: Space Telescope Science Inst.)
Mazzarella, J. M., & Boroson, T. A. 1993, ApJS, 85, 27
Mazzarella, J. M., Bothun, G. D., & Boroson, T. A. 1991, AJ, 101, 2034
Miller, J. S., & Goodrich, R. W. 1990, ApJ, 355, 456
Miyaji, T., Wilson, A. S., & Pérez-Fournon, I. 1992, ApJ, 385, 137
Morris, S., Ward, M., Whittle, M., Wilson, A. S., & Taylor, K. 1985, MNRAS, 216, 193
Mulchaey, J. S., Wilson, A. S., Bower, G. A., Heckman, T. M., Krolik, J. H., & Miley, G. K. 1994, ApJ, 433, 625
Nelson, C., & Whittle, M. 1995, ApJS, 99, 67
Nilson, P. 1973, Uppsala General Catalogue of Galaxies (Uppsala Astron. Obs. Ann., 6)
Osterbrock, D. E., & Dahari, O. 1983, ApJ, 273, 478
Pedlar, A., Dyson, J. E., & Unger, S. W. 1985, MNRAS, 214, 463
Phillips, M. M., Baldwin, J. A., Atwood, B., & Carswell, R. F. 1983, ApJ, 274, 558
Poulain, P. 1988, A&AS, 72, 215
Scoville, N. Z., Matthews, K., Carico, D. P., & Sanders, D. B. 1988, ApJ, 327, L61
Shlosman, I., Frank, J., & Begelman, M. C. 1989, Nature, 338, 45
Simkin, S. M., Su, H. J., & Schwarz, M. P. 1980, ApJ, 237, 404
Storchi-Bergmann, T., Wilson, A. S., & Baldwin, J. A. 1992, ApJ, 396, 45
Sutherland, R. S., Bicknell, G. V., & Dopita, M. A. 1993, ApJ, 414, 510
Taylor, D., Dyson, J. E., & Axon, D. J. 1992, MNRAS, 255, 351
Tohline, J. E., & Osterbrock, D. E. 1982, ApJ, 252, L49
Tran, H. D., Miller, J. S., & Kay, L. E. 1992, ApJ, 397, 452
Ulvestad, J. S., & Wilson, A. S. 1984, ApJ, 285, 439
———. 1989, ApJ, 343, 659
van Driel, W., & Buta, R. J. 1991, A&A, 245, 7
Veilleux, S. 1991a, ApJ, 369, 331
———. 1991b, ApJS, 75, 357
———. 1991c, ApJS, 75, 383
Veilleux, S., & Osterbrock, D. E. 1987, ApJS, 63, 295
Whittle, M. 1985, MNRAS, 213, 33
———. 1992a, ApJ, 387, 109
———. 1992b, ApJ, 387, 121
———. 1992c, ApJS, 79, 49
Whittle, M., et al. 1988, ApJ, 326, 125
Wilson, A. S., & Baldwin, J. A. 1989, AJ, 98, 2056
Wilson, A. S., Baldwin, J. A., Sun, S.-D., & Wright, A. E. 1986, ApJ, 310, 121
Wilson, A. S., Baldwin, J. A., & Ulvestad, J. S. 1985, ApJ, 291, 627
Wilson, A. S., Braatz, J. A., Heckman, T. M., Krolik, J. H., & Miley, G. K. 1993, ApJ, 419, L61
Wilson, A. S., Helfer, T. T., Haniff, C. A., & Ward, M. J. 1991, ApJ, 381, 79
Wilson, A. S., & Ulvestad, J. S. 1983, ApJ, 275, 8
———. 1987, ApJ, 319, 105
Wilson, A. S., & Willis, A. G. 1980, ApJ, 240, 429
Wray, J. D. 1988, The Color Atlas of Galaxies (Cambridge: Cambridge Univ. Press)